ARTICLE

Check for updates

Emergence of active turbulence in microswimmer suspensions due to active hydrodynamic stress and volume exclusion

Kai Qi [1,3], Elmar Westphal[2], Gerhard Gompper [1✉] & Roland G. Winkler [1✉]

Microswimmers exhibit an intriguing, highly-dynamic collective motion with large-scale swirling and streaming patterns, denoted as active turbulence – reminiscent of classical high-Reynolds-number hydrodynamic turbulence. Various experimental, numerical, and theoretical approaches have been applied to elucidate similarities and differences of inertial hydro-dynamic and active turbulence. We use squirmers embedded in a mesoscale fluid, modeled by the multiparticle collision dynamics (MPC) approach, to explore the collective behavior of bacteria-type microswimmers. Our model includes the active hydrodynamic stress generated by propulsion, and a rotlet dipole characteristic for flagellated bacteria. We find emergent clusters, activity-induced phase separation, and swarming behavior, depending on density, active stress, and the rotlet dipole strength. The analysis of the squirmer dynamics in the swarming phase yields Kolomogorov-Kraichnan-type hydrodynamic turbulence and energy spectra for sufficiently high concentrations and a strong rotlet dipole. This emphasizes the paramount importance of the hydrodynamic flow field for swarming motility and bacterial turbulence.

[1] Theoretical Physics of Living Matter, Institute of Biological Information Processing, and Institute for Advanced Simulation, Forschungszentrum Jülich, 52425 Jülich, Germany. [2] Peter Grünberg Institute and Jülich Centre for Neutron Science, Forschungszentrum Jülich, D-52425 Jülich, Germany. [3]Present address: CECAM Centre Européen de Calcul Atomique et Moléculaire, École Polytechnique Fédérale de Lausanne (EPFL), 1015 Lausanne, Switzerland. ✉email: g.gompper@fz-juelich.de; r.winkler@fz-juelich.de

Active matter comprises a unique class of systems with intricate structural and dynamical features, facilitated by their elementary agents consuming internal energy, or energy from the environment, to maintain an out-of-equilibrium state. The interplay between the autonomous locomotion of the agents and their interactions leads to large-scale self-organized swarm behavior manifested in such diverse biological systems as flocks of birds[1–4], school of fish[5,6], bacterial colonies[7–16], epithelial cell monolayers[17–19], and the cell cytoskeleton[20–23], as well as synthetic systems like robots[24,25], self-assembled magnetic spinners[26], and phoretic colloids[27–29].

Bacteria exhibit a particular mode of locomotion in dense populations denoted as *swarming motility*, where they exhibit rapid, coherent group migration over surfaces, with large-scale swirling and streaming patterns[7,10–12,30,31]. Similarly to bacterial swarming behavior[11,13,16,32–38], tissue cells[19,39–41], and filament/motor-protein mixtures[18,22,23,42,43] exhibit collective, visually chaotic motion, nowadays often denoted as *active turbulence* or *mesoscale turbulence*, with large-scale spatially and temporally random flow patterns. At first glance, the flow patterns are reminiscent of those observed in classical high-Reynolds-number hydrodynamic turbulence[44–46], despite active turbulence occurring at exceedingly small Reynolds numbers. The similarity prompted intensive studies of the collective motion of active matter systems to unravel the underlying physical mechanisms due to its prototypical character for nonlinear and none-quilibrium dynamical systems, which is considered as a major challenge for current theoretical physics[43].

Fundamental insight into hydrodynamic turbulence is achieved via velocity correlation functions[47]. In particular, Kolmogorov predicted the universal power-law dependence for the energy spectrum $E \sim k^{-\kappa}$ on the wavenumber $k = |\mathbf{k}|$, with $\kappa = 5/3$, obtained by Fourier transformation of the spatial velocity correlation function[44,47]. In fact, this relation applies for two- (2D) and three-dimensional (3D) systems[45]. Numerous studies on active systems reveal a wide spectrum of possible turbulent characteristics dependent on their constituents and the detailed (microscopic) interaction mechanisms, reflected in a wide range of exponents deviating from the Kolmogorov value, see Table 1. Experiments on *B. subtilis* and E. coli bacteria[13,38] yield exponents significantly above and below the Kolmogorov value. Computer simulations employing various models have been performed and the energy spectrum has been calculated. Non-hydrodynamic particle-based simulations of an extension of the Vicsek model[48], accounting for short-range parallel and large-range antiparallel alignment, yield the same exponent[49] as experiments on E. coli[13]. Simulations of self-propelled rodlike particles give a value close to the Kolmogorov value[13,50]. Lattice

Boltzmann simulations of microswimmers represented by extended force dipoles (point particles) produce seemingly turbulent behavior for sufficiently large swimmer densities[51] (see Table 1). For active nematics, the route to chaotic behavior has been studied experimentally and theoretically[23,52]. Their dynamics is characterized by an intrinsic length scale l_a, where l_a is determined by the balance between the active and nematic elastic stress[18,42], and the creation and annihilation of topological defects. In addition, various theoretical studies have been performed with[42] and without[18] defects, where both yield similar energy spectra with distinct power-law exponents for length scales larger and smaller than l_a (Table 1). In contrast, we expect hydrodynamic interactions to dominate the chaotic and turbulent behavior in bacterial suspensions. Hence, it is a priori not evident that both types of chaotic dynamics exhibit the same kind of turbulent behavior, taken into account the disparity in the exponents κ and $\hat{\kappa}$ in Table 1.

There are two particular systems of mesoscopic active particles, namely spinners — short rodlike self-organized colloidal structures rotated by an external magnetic field[53] — and Marangoni surfers[28], where turbulent dynamics consistent with Kolmogorov scaling has been observed. Their Reynolds numbers $Re \sim \mathcal{O}(10)$ are much smaller than that of classical inertial turbulence, but are much larger than those of microswimmer systems, where $Re \ll 1$.

As a major difference to hydrodynamic turbulence, various experimental and simulation studies of active turbulence suggest the presence of a characteristic upper length scale for the vortex size, only below which the energy spectrum decreases in a power-law manner with increasing wavenumber k[32,35,36]. This scale is typically on the order of ten microswimmer lengths. Theoretical studies based on a continuum approach[13,36,43,54], where the velocity field is described by the incompressible Toner-Tu equation[55,56] combined with a Swift-Hohenberg term[57] for pattern formation, support this observation. However, in contrast to high-Reynolds-number hydrodynamic turbulence, which is governed by inertia, the internal stress due to self-propulsion and polar alignment interactions of the active agents is important, which, combined with the fluid dynamics, determines the vortex size[54].

The diversity of obtained energy spectra and characteristic power laws (Table 1) indicates a strong dependence of the collective behavior on the detailed microswimmer interactions. Yet, it is not clear to which extent and under what circumstances hydrodynamic interactions are important.

In this article, we perform extensive coarse-grained mesoscale hydrodynamic simulations by employing the multiparticle collision dynamics (MPC) approach for fluids[58–60] to elucidate the collective, turbulent motion of microswimmers in monolayer

Table 1 Various aspects of experimentally, theoretically, and by simulations studied systems exhibiting features of active turbulence.

Technique	System/Approach	Shape	HI	Excl. volume	Active stress	Rotlet dipole	Gaussian vel. distr.	κ, $k^{-\kappa}$ (large k)	$\hat{\kappa}$, $k^{\hat{\kappa}}$ (small k)	Ref.
Experiment	*B. subtilis*	Elong.	✓	✓	✓	✓	✓	8/3	5/3	13
	E. coli	Elong.	✓	✓	✓	✓	/	4/3	3/5	38
	Cells	Elong.	✓	✓	✓	—	—	≳13/3	—	41
Theory	Field, isotrop.	/	✓	—	—	—	/	8/3	5/3	13
	Act. nem. (def. free)	/	✓	—	—	—	/	12/3	−1	18
	Act. nem.	/	✓	—	—	—	✓	12/3	−1	42
Simulations	SPR	Rod	—	✓	—	—	✓	≳5/3	/	50
	Vicsek-type	Point part.	—	—	(✓)	—	/	8/3	5/3	49
	LB	Point part.	✓	—	✓	—	/	11/3	/	51
	MPC: $\phi = 0.60$	Spheroid	✓	✓	✓	✓	—	2	5/3	This work
	MPC: $\phi = 0.68$	Spheroid	✓	✓	✓	✓	—	5/3	1	This work

The articles (Ref.) discuss microscale systems exhibiting a power-law energy spectrum $E(k) \sim k^{-\kappa}$ for $k_m < k < k_c$ and $E(k) \sim k^{\hat{\kappa}}$ for $k < k_m$, with k_m and k_c the wavenumber of the maximum in the energy spectrum and that of the microswimmer characteristic length, respectively. Note that in active nematic theory, $k_m = 2\pi/l_a$[18,42]. Cells comprise canine kidney, endothelial, myoblast, and fibroblast cells.
Symbols: "✓" aspect is present, "—" aspect is absent, "/" aspect has not been analyzed/considered.
Act. nem. active nematics, *SPR* self-propelled rod, *LB* Lattice Boltzmann, *MPC* multiparticle collision dynamics, *HI* hydrodynamic interactions, ϕ packing fraction.
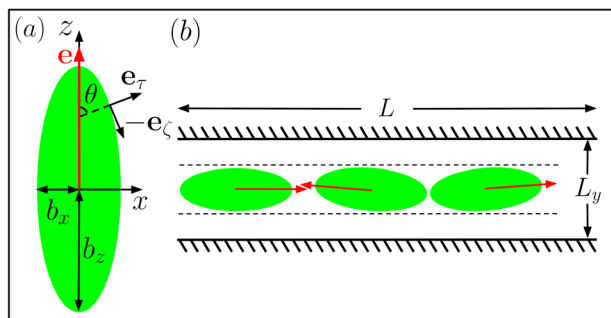
Fig. 1 Illustration of the simulation setup. a Sketch of a spheroidal squirmer, which is propelled in the direction **e** (red arrow) along the z-axis of the body-fixed reference frame. The spheroid's semi-major- and -minor axis are b_z and b_x, respectively, and $\mathbf{e}_\tau$ and $\mathbf{e}_\zeta$ indicate the local normal and tangential unit vectors. **b** Multiple spheroidal squirmers in a narrow square-shaped slit of width $L_y = 4b_x$ and lateral extension L. A strong repulsive wall potential, as indicated by the dashed lines, implies quasi-2D confinement in the channel center.

films. The microswimmers are described in a coarse-grained manner through the squirmer model[60–64]. Particular attention is paid to the influence of the microswimmers' hydrodynamic flow field on their collective behavior, i.e, the active stress and the rotlet dipole resulting from the rotating flagella (bundles) and the counterrotating cell body in flagellated bacteria[65–68]. In general, hydrodynamics plays a decisive role in the collective behavior of microswimmers[60,63,69]. While dry spherical active Brownian particles (ABPs) exhibit motility-induced phases separation (MIPS)[15,70–75], spherical microswimmers in the presence of hydrodynamics show cluster formation[60], but no phase separation[60,76]. However, anisotropic, spheroidal squirmers exhibit enhanced clustering compared to similar ABP systems due to hydrodynamic attraction and steric interactions[60]. Hence, it is important to unravel the effect of shape, active stress, and of a rotlet dipole in dense microswimmer systems on their emergent collective properties, since bacteria in films exhibit swarming — a rapid, coherent group migration over surfaces in dense populations, with large-scale swirling and streaming patterns[10,11,16,31] — rather than clustering and phase separation[11,13,16,32–36,38].

By systematically varying the squirmer density, the active stress, and the rotlet dipole strength, our simulations provide insight into their influence on the collective dynamics of microswimmers. In particular, the combination of active stresses and a non-zero rotlet dipole suppresses phase separation and promotes swarming motility.

The analysis of the swarming phases reveals turbulent-like motion, where the energy spectrum displays power-law decays below the characteristic length scale discussed above, however, with an exponent depending on the squirmer concentration. We find the value $\kappa = 5/3$ for our largest density, strong active stress, and a non-zero rotlet dipole, consistent with the Kolmogorov prediction. Based on our analysis, in the Discussion and Conclusions section, we propose criteria which a dense, visually chaotic systems should satisfy to be possibly classified as turbulent.

Results

In our simulations, N_{sq} prolate spheroidal squirmers with the semi-major, b_z, and -minor, b_x, axis are confined in a three-dimensional narrow slit between two parallel walls and periodic boundary conditions along the x and z direction (Fig. 1). As described in the Methods section, the prescribed squirmer surface velocity yields
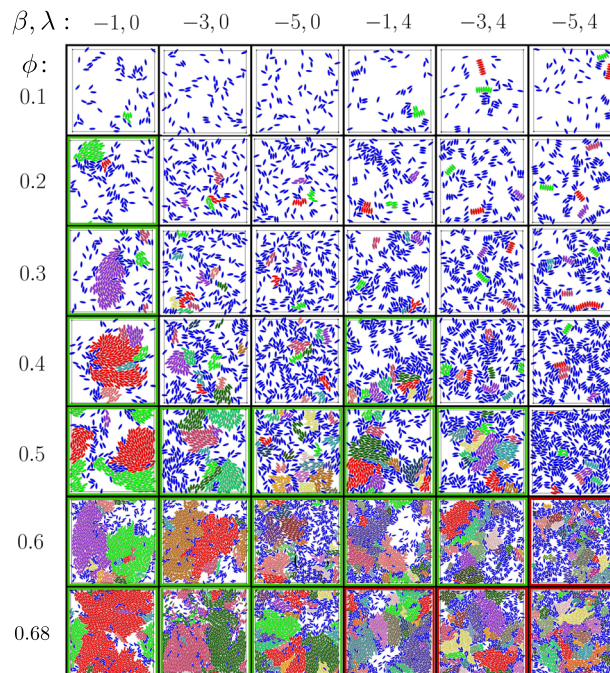
Fig. 2 Snapshots of emergent structures. Structures of squirmers for various packing fractions, ϕ, active stresses, β, and rotlet dipole strengths, λ. The box sizes are $L = 160a$ for $\phi \leq 0.5$ and $L = 230a$ for $\phi > 0.5$. Small clusters with squirmer numbers $m \leq 4$ are colored in blue, various other (random) colors are used for clusters with $m > 4$. The snapshots with green frames correspond to (large) clusters and A-MIPS, where clusters are systems-spanning at higher packing fractions (see Supplementary Movie 1 and Supplementary Movie 2). The snapshots with red frames correspond to swarming systems (see Supplementary Movie 3). The other systems show individually squirmers and (few) small clusters (see Supplementary Movie 4).

swimming with the velocity v_0, an active stress of strength β, and a rotlet dipole of strength λ. The embedding fluid is explicitly modeled via the multiparticle collision dynamics (MPC) method[58,59], applying the stochastic-rotation variant with angular momentum conservation (MPC-SRD+a)[77,78]. Further details of the model and implementation are presented in the Methods section.

Structural properties. The simulation snapshots of Fig. 2 illustrate emergent structures for the various considered packing fractions, active stresses, and rotlet dipole strengths. Distinct motility patterns can be identified:

(i)   Gas of small clusters for $\phi \lesssim 0.3$.
(ii) Motility-induced phase separation (A-MIPS) for $|\beta| \geq 1$, $\lambda = 0$, $\phi \gtrsim 0.3$. Since here the shape of the spheroids implies squirmer alignment and the formation of polar motile clusters, we use the notation A-MIPS to distinguish it from the case of isotropic, non-aligning particles, which form immobile clusters (MIPS)[15,71,72].
(iii) Swarming motility for $|\beta| > 1$, $\lambda = 4$, $\phi \gtrsim 0.6$.
      In a general sense, the clusters formed by A-MIPS can exhibit swarming behavior, because they are rather dynamic and exhibit translational and rotational motion. Their size increases with increasing packing fraction and are system-spanning for $\phi \gtrsim 0.5$, consistent with our previous studies[60].

In the dense swarming phase, clusters of squirmers migrate collectively, thereby forming dynamic swirling and streaming patterns[10,12,16,31]. A quantitative criterion for the classification
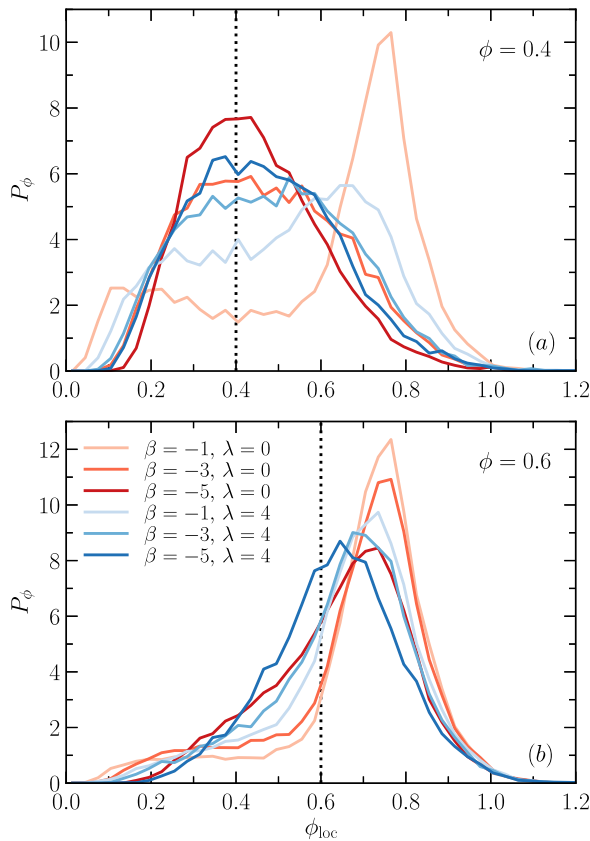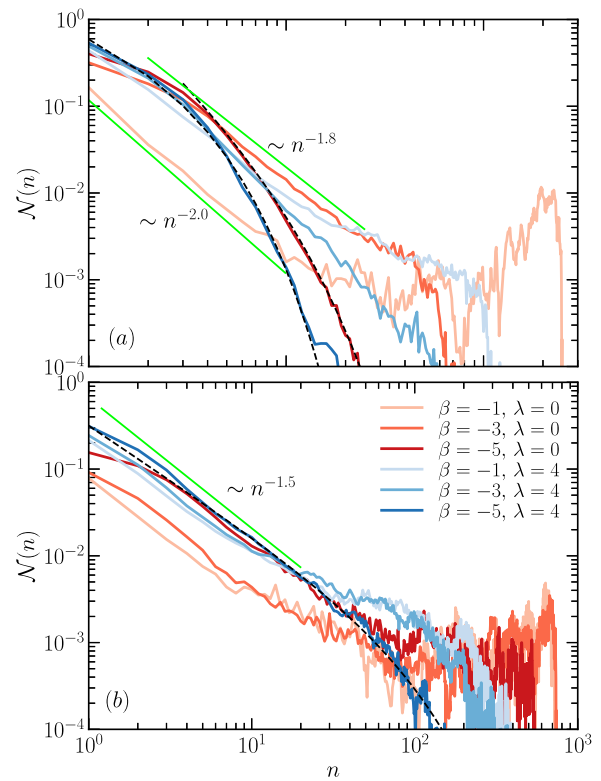
Fig. 3 Local packing fraction. Probability distribution P_ϕ of the local packing fractions ϕ_{loc} for the average area packing fraction (**a**) $\phi = 0.4$ and (**b**) $\phi = 0.6$ (vertical dotted lines). The various curves correspond to $\beta = -1$, -3, and -5 (bright to dark), and $\lambda = 0$ (red) and $\lambda = 4$ (blue), respectively.

Fig. 4 Cluster-sizer distribution function. Cluster-size distribution function $\mathcal{N}(n)$ (Eq. (1)) for the average packing fractions (**a**) $\phi = 0.4$ and (**b**) $\phi = 0.6$. The curves present results for $\beta = -1$, -3, and -5 (bright to dark) and $\lambda = 0$ (red) and $\lambda = 4$ (blue), respectively. The dashed lines are fits of the function $\mathcal{N}(x)$ of Eq. (2) with the parameters of Table 2. The green solid lines indicate power laws with the respective exponents.

into A-MIPS and swarming motility will be provided in terms of the cluster-size distribution function (cf. Sec. Cluster-size distribution). Some of the small clusters for $\phi \lesssim 0.3$ exhibit cooperative motion, where a few squirmers move together for some time. In general, the rotlet dipole enhances cluster formation, and squirmers align side by side, which is clearly visible for $\phi \lesssim 0.4$. The precise mechanism for this cooperative motion is unexplored, but could depend on squirmer wall interactions. In contrast, for larger packing fractions the rotlet dipole suppresses A-MIPS and enhances swarming motility.

Local packing fraction. Clustering and A-MIPS of the squirmers are analyzed quantitatively by a Voronoi tessellation of the accessible volume[60,74,79,80]. Figure 3 provides examples of density distributions for the average packing fractions $\phi = 0.4$ and 0.6. The pronounced peak at the local packing fraction $\phi_{loc} \approx 0.75$ for $\phi = 0.4$, $\beta = -1$, and $\lambda = 0$ indicates A-MIPS (Fig. 3(a)), with a dense phase in contact with a dilute phase, consistent with the snapshots of Fig. 2. Results for large $|\beta|$ imply a disintegration of the large aggregate and ultimately, for $\beta < -3$, P_ϕ displays a maximum at the average packing fraction, which indicates the absence of phase separation. Similarly, at $\phi = 0.6$, the peaks in Fig. 3(b) for $\lambda = 0$ indicate phase separation, even for β as negative as $\beta = -5$. The rotlet dipole prevents formation of large clusters, but even for $\beta = -5$ and $\lambda = 4$ a broad range of cluster sizes exists.

Cluster-size distribution. The cluster-size distribution function

$$\mathcal{N}(n) = \frac{1}{N_{sq}} n p(n) \qquad (1)$$

represents the fraction of squirmers belonging to a cluster of size n, where $p(n)$ is the number of clusters of size n. The distribution is normalized such that $\sum_{n=1}^{N_{sq}} \mathcal{N}(n) = 1$. We use a distance and an orientation criterion to define a cluster: a squirmer belongs to a cluster, when its closest distance to another squirmer of the cluster is $d_s < 1.8(2^{1/6} - 1)\sigma_s$ and the angle between the orientations of the two squirmers is $< \pi/6$ (see Methods section for the definition). The latter allows us to identify different clusters even at high packing fractions.

The cluster-size distribution function is a useful quantity to characterize the motility pattern of a microswimmer system[16,81]. In the homogeneous phase, the distribution function decays exponentially, whereas a second peak (bimodal distribution) indicates the formation of giant clusters (A-MIPS). At the percolation transition, $\mathcal{N}$ becomes scale free and decays by a power law, $\mathcal{N} \sim x^{-\gamma}$[81]. The swarming phase is characterized by a power-law decay with an exponential cut-off and a characteristic scale determined by an average vortex size[16]. The distribution functions presented in Fig. 4 confirm our above conclusions on the emergent phases and motility patterns.

For $\phi = 0.4$ and $(\beta, \lambda) = (-1, 0)$, $(-1, 4)$, $\phi = 0.6$, $\lambda = 0$, and all considered β, as well as $(\beta, \lambda) = (-1, 4)$, $(-3, 4)$, we obtain bi- and multimodal distributions with a power-law decay (cf. Table 2) at small cluster sizes and a high probability for giant clusters ($N_{sq} = 270$, $\phi = 0.4$ and $N_{sq} = 833$, $\phi = 0.6$). This indicates A-MIPS[16,60]. The large polar clusters are mobile, but the systems lack the characteristic large-scale swirling patterns of swarming (cf. Supplementary Movie 1 and Supplementary Movie 2). The distribution functions for $\phi = 0.4$, $(\beta, \lambda) = (-5, 0)$, $(-5, 4)$ decay in a qualitative different manner. They are well fitted by the

Table 2 Fit parameters of cluster-size distribution.

ϕ	β	λ	A	x_1	γ	Mode
0.4	−1	0	0.17	/	2.0	A-MIPS
0.4	−3	0	0.86	/	1.8	
0.4	−5	0	0.75	1.38	0.31	Clus. gas
0.4	−1	4	0.5	/	1.8	A-MIPS
0.4	−3	4	1.25	/	2.3	
0.4	−5	4	0.98	2.0	0.7	Clus. gas
0.6	−1	0	0.08	/	1.5	A-MIPS
0.6	−3	0	0.14	/	1.5	A-MIPS
0.6	−5	0	0.34	/	1.4	A-MIPS
0.6	−1	4	0.22	/	1.4	A-MIPS
0.6	−3	4	0.27	/	1.4	A-MIPS
0.6	−5	4	0.32	80	1.25	Swarming

Parameters of the cluster-size distribution function, Eq. (2), for various average squirmer densities, active stresses, and rotlet dipole strengths. "/" indicates absence of the exponential function, i.e., $\mathcal{N} = Ax^{-\gamma}$. The last column classifies the systems according to their structures and collective behavior. No entry indicates inconclusive behavior.
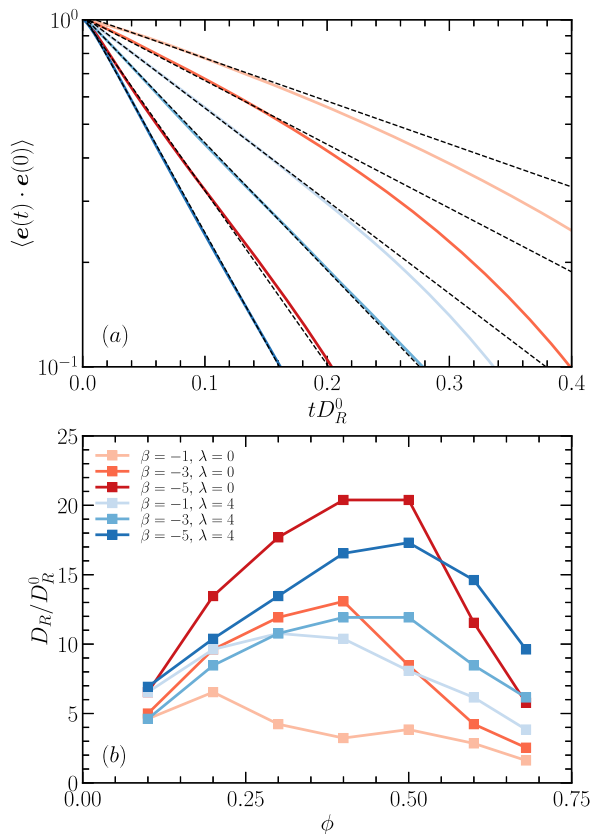
Fig. 5 Propulsion direction autocorrelation function. a Autocorrelation function of the propulsion direction as a function of time for the packing fraction $\phi = 0.6$. D_R^0 is the rotational diffusion coefficient of an individual squirmer in the slit (see Methods). The dotted lines are fits to Eq. (3). **b** Diffusion coefficients, D_R, obtained by a fit of Eq. (3) as a function of the average packing fraction ϕ. The curves indicate results for $\beta = -1, -3$, and -5 (bright to dark) and $\lambda = 0$ (red) and $\lambda = 4$ (blue), respectively.

function[82]

$$\mathcal{N}(x) = Ax^{-\gamma}e^{-x/x_1}. \tag{2}$$

This functional form is observed in various cluster-forming processes[81]. The function interpolates between the power-law decay found for percolating clusters and an exponential suppression of larger clusters. Table 2 presents the fit parameters

for the various curves of Fig. 4. The exponential large-n decay for $\phi = 0.4$, $(\beta, \lambda) = (-5, 0), (-5, 4)$ with a small value of x_1 reflects the predominance of very small clusters — such systems are considered as a gas of clusters. In contrast, the cluster-size distribution for $\phi = 0.6$, $(\beta, \lambda) = (-5, 4)$ decreases over a broad range of n in a power-law fashion reflecting the presence of a wide distribution of cluster sizes ($x_1 \approx 80$), and only larger clusters are exponentially suppressed — this system is in the swarming phase. The major difference to systems with $(\beta, \lambda) = (-1, 4)$, $(-3, 4)$ at this concentration is the more pronounced suppression of large clusters, which renders the overall system more dynamic.

The probability distribution functions of the local packing fraction (Fig. 3) and cluster-size distribution functions (Fig. 4) clearly reveal a marked effect of the rotlet dipole on the collective behavior of the squirmers. In particular, A-MIPS is suppressed, but formation of highly dynamic clusters prevails, with a rather broad distribution of cluster sizes for high squirmer densities.

Dynamical properties

Rotational diffusion. An individual squirmer in the slit exhibits rotational diffusion around a minor body axis. Interactions between squirmers, either steric or by their flow fields, change their diffusive behavior substantially[60,63]. Figure 5(a) displays the time dependence of the autocorrelation function $\langle \boldsymbol{e}(t) \cdot \boldsymbol{e}(0) \rangle$ of the propulsion direction of the squirmers. The various curves reflect a marked dependence of the rotational dynamics on the active stress and the rotlet dipole strength. The correlation function of the systems for $(\beta, \lambda) = (-1, 0), (-3, 0), (-1, 4)$ exhibit a non-single-exponential decay. Steric interactions between squirmers with a preference to cluster formation as well as between finite-size clusters lead to a rotation of whole clusters, which implies a faster decay of the rotational correlation compared to thermal fluctuations alone (cf. Supplementary Movie 4)[83].

We characterize the rotational motion by fitting the initial decay of the correlation function with the exponential

$$C_R(t) = \langle \boldsymbol{e}(t) \cdot \boldsymbol{e}(0) \rangle = C_R^0 e^{-D_R t}, \tag{3}$$

as displayed in Fig. 5(a). The factor $C_R^0 \approx 1.03$ is included to account for a non-exponential decay for very short times. Squirmers with large active stresses and a rotlet dipole ((β, λ) = $(-5, 0), (-3, 4), (-5, 4)$) exhibit an exponentially decaying correlation function C_R over more than an order of magnitude. The extracted rotational diffusion coefficients D_R obey $D_R/D_R^0 > 1$ (Fig. 5(b)), which reveals an accelerated rotational motion by shape-induced steric interactions and hydrodynamic flow fields. Note that D_R^0 in a dilute system is independent of β. The diffusion coefficient D_R increases with increasing squirmer concentration, reaches a packing fraction-dependent maximum and decreases again for larger ϕ. The snapshots of Fig. 2 suggest that the maxima in Fig. 5(b) are related to the threshold of cluster formation. An increasing number of squirmer contacts with increasing ϕ ($\phi \lesssim 0.5$) implies a faster reorientation. However, at larger ϕ, the emerging clusters, which move collectively and more persistently, lead to a reduction of D_R. The larger D_R values for larger $|\beta|$ demonstrate the substantial contribution of active stress to the reorientation of the squirmers. At smaller ϕ and $\beta < -1$, the presence of a rotlet dipole with $\lambda = 4$ evidently reduces D_R compared to that for $\lambda = 0$, which is associated with the appearance of small clusters of side-by-side swimming squirmers (cf. Fig. 2 and Supplementary Movie 4). In contrast, at high packing fractions, a rotlet dipole implies a larger D_R as a consequence of an enhanced orientational motion of smaller clusters, specifically at large $|\beta| = 5$.
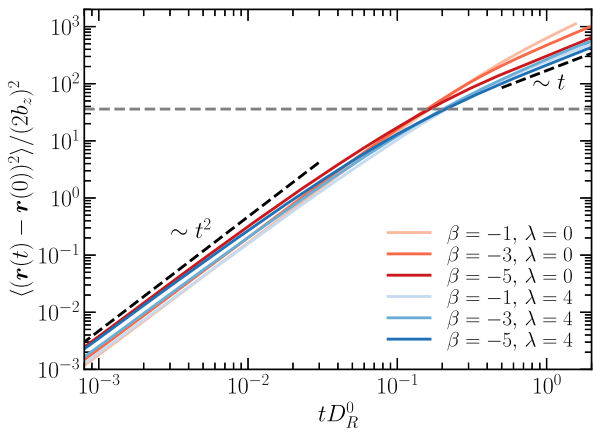
Fig. 6 Mean-square displacement. Mean-square displacement of the square center of mass $\mathbf{r}(t)$ as a function of time for the packing fraction $\phi = 0.6$, various active stresses β, and rotlet-dipole strengths λ. D_R^0 is the rotational diffusion coefficient of an individual squirmer and b_z the major-semi axis of the spheroid. The black dashed lines indicate the power laws of ballistic (t^2) and diffusive (t) motion, respectively. The horizontal gray dashed line corresponds to the displacement of 6 squirmer lengths.

Mean square displacement. The mean-square displacement of the squirmers at high packing fractions ($\phi \geq 0.6$, Fig. 6) exhibit the typical ballistic motion for short times and a crossover to a diffusive motion for long times $tD_R^0 \gtrsim 0.1$[15,71], at least for systems with $\lambda = 4$. (The resolution of the long-time behavior of the phase separated systems for $\lambda = 0$ requires longer simulations.) There is only a slight difference in the swimming speed of the various squirmers at short times. The presence of a rotlet dipole causes an earlier deviation from a strict ballistic motion toward a ballistic-like motion with an exponent somewhat smaller than 2 as time increases compared to squirmers without such a dipole. The systems with $(\beta, \lambda) = (-5, 0), (-1, 4), (-3, 4), (-5, 4)$ exhibit a crossover from a ballistic or near ballistic to a diffusive motion at a displacement roughly corresponding to $12b_z$, i.e., 6 squirmer lengths. We may consider this as a characteristic length scale in the system, separating the scale of persistent motion from that of diffusive motion. The crossover for $(\beta, \lambda) = (-1, 0), (-3, 0)$ occurs at longer times.

The attempt to fit the mean-square displacement of Fig. 6 by the expression of an ABP[15,71] failed for $\beta > 1$, in particular for $\lambda = 4$. As reflected by the density dependence of D_R, the long-time dynamics is strongly affected by the formation of cluster and their collective dynamics. However, the restriction of the fit to the crossover regime from ballistic to diffusive motion yields rotational diffusion coefficients in agreement with those extracted from the short-time behavior of the correlation function C_R (Fig. 5).

Velocity distribution function. Thermal fluctuations and squirmer interactions imply strongly varying instantaneous velocities, both in direction as well as in magnitude. Hence, for the calculation of the velocity distribution function, we determine a swimming velocity by the finite-difference quotient of displacements

$$\mathbf{v}_i(t) = \frac{\mathbf{r}_i(t) - \mathbf{r}_i(t - \Delta t)}{\Delta t}, \qquad (4)$$

where $\mathbf{r}_i$ is the center-of-mass position of squirmer i. During the selected time interval $\Delta t = 10^3\sqrt{ma^2/(k_BT)}$, a squirmer moves at most the distance $2b_z/3$.

For lower packing fractions $\phi \leq 0.5$, Fig. 7(a) displays the distribution function $P(\mathbf{v})$ of the Cartesian in-plane velocities
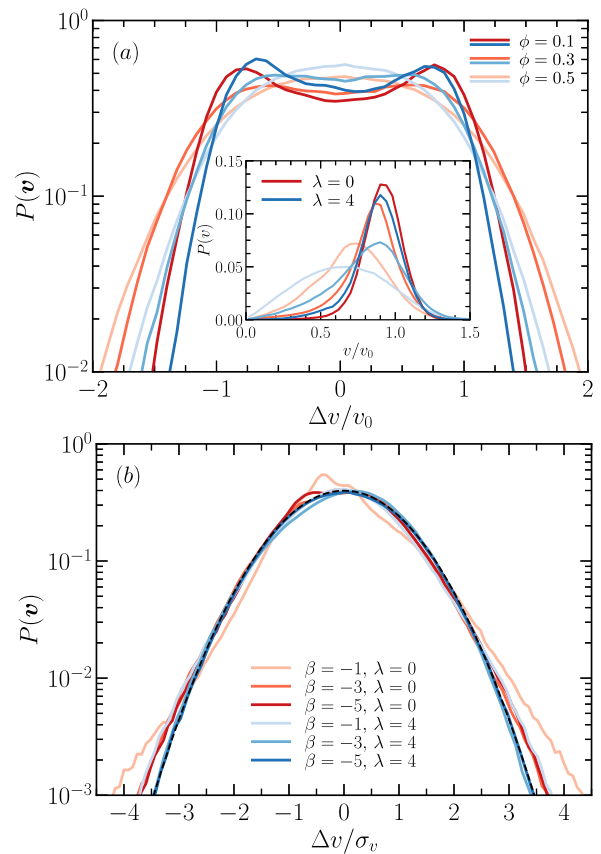

Fig. 7 Velocity distribution function. a Distribution function $P(\mathbf{v})$ of the Cartesian in-plane velocity components $\Delta v = v_{x/z} - \bar{v}_{x/z}$, with respect to the mean velocity $\bar{v}_{x/z}$, normalized by the swimming speed v_0 for the active stress $\beta = -5$, the indicated packing fractions ϕ, and the rotlet-dipole strengths $\lambda = 0, 4$. Inset: distribution function $P(v)$ of the modulus $v = |\mathbf{v}|$ of the velocity for $\beta = -1$. **b** Distribution function of the Cartesian in-plane velocity components normalized by the standard deviation σ_v for $\phi = 0.68$ and various β and λ. The dashed line is a Gaussian of unit variance.

$\Delta v = (v_{x/z} - \bar{v}_{x/z})$, where $\bar{v}_{x/z}$ are the ensemble- and time-averaged velocities along the Cartesian directions x and z. The averages $\bar{v}_{x/z}$ are very small for all considered parameter sets. Since the two spatial dimensions are equivalent, $P(\mathbf{v})$ is averaged over the x and z direction. For $\phi = 0.1$, we find pronounced non-Gaussian, bimodal distributions. It reflects the swimming of the squirmers with nearly constant velocity magnitude v_0 along their major semi-axis. This is emphasized by the distribution function of the velocity modulus $v = |\mathbf{v}|$ (inset Fig. 7(a)). This behavior is not unique for squirmers, but generic and also displayed by ABPs[84]. Thermal fluctuations, and hydrodynamic and steric interactions between squirmers modify the swimming velocity, hence, $P(\mathbf{v})$ is broadened and asymmetric with respect to the average of the modulus of the swimming velocity. With increasing density, the modulus decreases and the two peaks of the bimodal distribution gradually merge, exhibiting a flat central regime for certain parameters. Our data show that the rotlet dipole enhances the variations in v.

At the highest packing fraction $\phi = 0.68$, compare Fig. 7(b), in particular for $(\beta, \lambda) = (-5, 4)$, the squirmers strongly interact with each other and the distribution function $P(\mathbf{v})$ becomes Maxwellian and $P(\mathbf{v})$ Gaussian. The latter not only requires pronounced changes of the swimming direction, but more importantly, of the modulus v. The crossover from a bimodal to a Gaussian distribution is gradual and depends on the
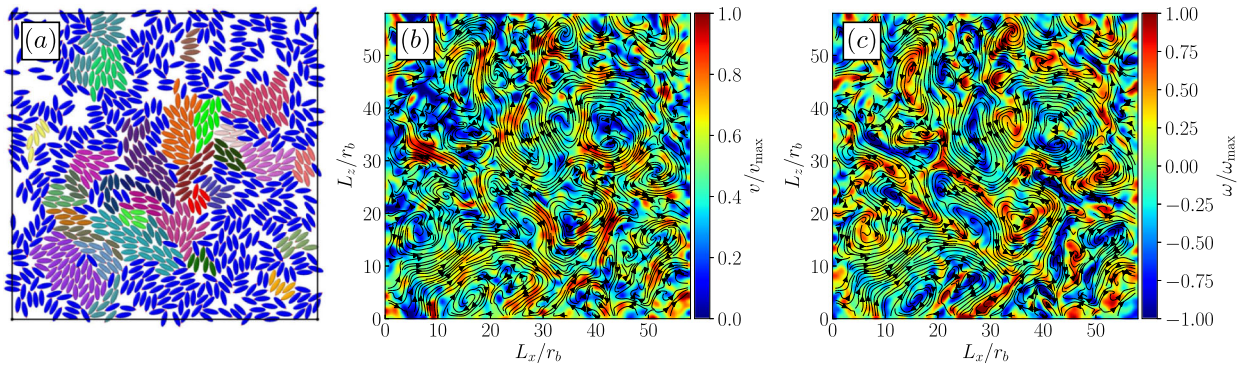
Fig. 8 Squirmer flow fields. Visual chaotic collective dynamics of squirmers. **a** Snapshot illustrating the presence of clusters. **b** Velocity field $v(\mathbf{r}, t)$ and **c** vorticity field $\omega(\mathbf{r}, t) = \partial v_z/\partial x - \partial v_x/\partial z$ of the system with $N_{sq} = 833$ squirmers, $\beta = -5$, $\lambda = 4$, and the packing fraction $\phi = 0.6$. The black lines with arrows indicate the streamlines of the fields (See Supplementary Movie 3, Supplementary Movie 5, and Supplementary Movie 6). The maximum values of the flow fields are $v_{max} = 6 \times 10^{-3} \sqrt{k_B T/m}$ and $\omega_{max} = 1.2 \times 10^{-3} \sqrt{k_B T/(ma^2)}$, corresponding to the effective Péclet number $Pe = 96$ and $\omega_{max}/(2\pi D_R^0) = 38$, and $r_b = 2b_x = 4a$, the diameter of the minor axis. For the velocity field, squirmer velocities (Eq. (4)) are averaged over 60 subsequent configurations separated by the time interval $10^2 \sqrt{ma^2/(k_B T)}$ and sorted into quadratic bins of length r_b. The vorticity field is calculated by the five-point stencil method.
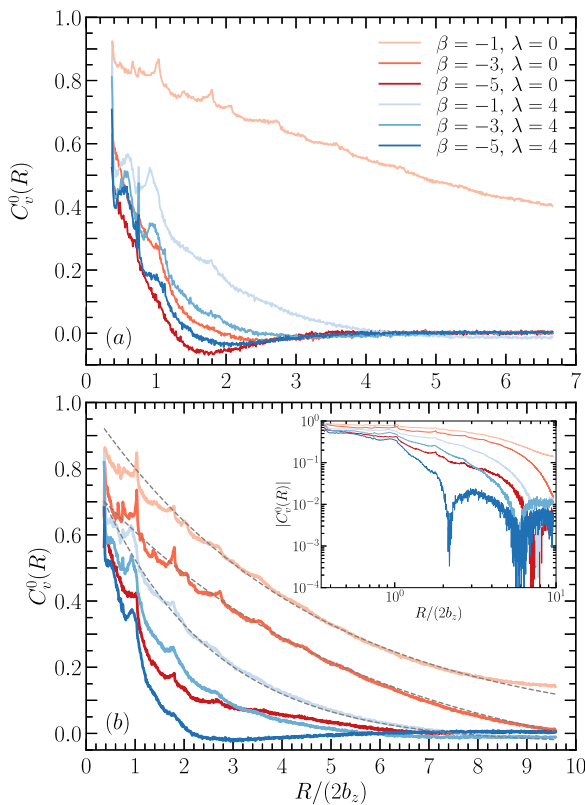
Fig. 9 Velocity correlation function. Normalized spatial velocity correlation function $C_v^0(R)$ for the packing fraction (**a**) $\phi = 0.4$ and (**b**) $\phi = 0.6$ as a function of the radial distance $R/(2b_z)$, where b_z is the semi-major axis of the spheroid, various active stresses β, and rotlet-dipole strengths λ. The inset in **b** displays C_v^0 in log-log representation. Dashed lines are fits to Eq. (5). Note that the peaks for $R/(2b_z) \approx 1, 2, \ldots$ reflect the local packing of the squirmers.

for a strongly correlated dynamics of squirmers in huge clusters (Fig. 2), with a very slow sampling of the velocity distribution. As a consequence, we obtain broad tails and large variations in the vicinity of $\Delta v = 0$ in the distribution function. Here, many more realizations and longer simulation times have to be considered to converge to the final stationary state. It is worth mentioning that experimental and theoretical studies of persistent random walks with a broad distribution of relaxation times predict non-Gaussian distribution functions with a broad tail[85,86]. Indeed, the orientational correlation function of the squirmers decays in a non-single exponential manner for various pairs of β and λ, specifically for $\lambda = 0$, corresponding to a wide distribution of rotational diffusion coefficients, as shown in Fig. 5(a). This reflects a more intricate dynamics of the squirmers in these systems, which could suffice to result in non-Gaussian velocity distribution functions. Here, further studies are required to resolve the influence of clusters on the dynamics of the squirmers and the velocity distribution function.

We like to emphasize that the velocity distribution functions in the regime of swarming motility, especially for systems with $\phi = 0.68$ and $(\beta, \lambda) = (-3, 4), (-5, 4)$, are very well described by a Gaussian, despite pronounced collective swimming. Evidently, steric and flow-field interactions induce sufficient randomness, which correspondingly leads to large variations in the swimming velocity, specifically in the modulus. This aspect is particularly relevant, because velocities in both bacterial[13,36] and high-Reynolds-number turbulence are Gaussian distributed.

Active turbulence. The characteristic features of the swimmer flow fields at higher densities are illustrated in Fig. 8. The clusters depicted in Fig. 8(a) exhibit a visually chaotic collective motion with regions of low and high velocity (Fig. 8(b)) and vorticity (Fig. 8(c)) (see Supplementary Movie 3, Supplementary Movie 5, and Supplementary Movie 6 for the packing fraction $\phi = 0.68$). The patterns are similar to those observed in experiments on bacteria[13,16,32,35,36], previous simulations[13,49], and continuum theory[13,33,36].

Spatial velocity correlation function. Quantitative insight into the turbulent dynamics of the squirmers is obtained by their spatial velocity correlation function, a concept well established in classic hydrodynamic turbulence[13,44,46,47]. For the discrete particle

microswimmer parameters β and λ. The broad tails of the distribution functions for $\lambda = 0$ and the small deviations from a Gaussian for $\beta = -3$ and -5 reflect a persistent motion of squirmers in large clusters with a preference toward larger velocities v. The system with $(\beta, \lambda) = (-1, 0)$ provides an example

Table 3 Fit parameters of velocity correlation function.

β	λ	A_v	$\xi/(2b_x)$	g
−1	0	1.00	4.5	0.00
−3	0	0.92	5.6	0.16
−1	4	0.86	2.3	0.032

Parameters of the spatial velocity correlation function, Eq. (6), for various active stresses and rotlet dipole strengths, and the squirmer density $\phi = 0.6$.

system, we define the spatial velocity correlation function as[50,74,87]

$$C_v(\mathbf{R}) = \frac{\left\langle \sum_{i,j\neq i} \mathbf{v}_i(t) \cdot \mathbf{v}_j(t) \delta(\mathbf{R} - |\mathbf{r}_i - \mathbf{r}_j|) \right\rangle}{\left\langle \sum_{i,j\neq i} \delta(\mathbf{R} - |\mathbf{r}_i - \mathbf{r}_j|) \right\rangle}. \tag{5}$$

Moreover, we introduce a normalized velocity correlation function as $C_v^0(R) = C_v(R)/c_0$, with $c_0 = \sum_i \langle \mathbf{v}_i^2 \rangle / Nsq$. (For a homogeneous and isotropic system, $C_v(R)$ is a function of $R = |\mathbf{R}|$ only.) Results of C_v^0 for the packing fractions $\phi = 0.4$ and 0.6 are presented in Fig. 9. Three distinct decay patterns can be identified: (i) a very slow decay over roughly the whole system ($\phi = 0.4$, $(\beta, \lambda) = (-1, 0)$, Fig. 9(a); $\phi = 0.6$, $(\beta, \lambda) = (-1, 0), (-3, 0)$, Fig. 9(b)), (ii) a decay, where correlations functions are negative for $R \lesssim L/2$ ($\phi = 0.4$, $(\beta, \lambda) = (-1, 4)$; $\phi = 0.6$, $(\beta, \lambda) = (-1, 4)$, $(-3, 4)$), and (iii) correlations functions, which assume negative values over a certain interval, but are positive for $R \approx L/2$ ($\phi = 0.4$, $(\beta, \lambda) = (-5, 0), (-3, 4), (-5, 4)$; $\phi = 0.6$, $(\beta, \lambda) = (-5, 4)$). The case (i) corresponds to long-range correlations over the entire simulation box, consistent with A-MIPS and the appearance of a large cluster (Fig. 4). As shown in Fig. 9(b), such $C_v^0(R)$ can be fitted by the function

$$C_v^0(x) = A_v e^{-x/\xi} - g. \tag{6}$$

Specifically for $\phi = 0.6$, we obtain the parameters of Table 3. The respective velocity correlation functions decay approximately exponentially, with characteristic lengths scales between 2.3 and 5.6 swimmer lengths. The smaller value $\xi/(2b_z) = 2.3$ for $\lambda = 4$ indicates that a non-zero rotlet dipole implies weaker spatial correlation and, hence, smaller clusters. The distinct decay patterns support our conclusion on the motility mode as discussed in relation with the cluster-size distribution functions (Fig. 4). However, a clear-cut separation of swarming and cluster dynamics is difficult to establish based on $C_v(R)$.

An important feature of bacterial turbulence is a finite vortex size, which marks a characteristic length scale in the system and is reflected in a minimum of the velocity correlation function[13,34,36,87]. Our simulations yield such a minimum, e.g., for $\phi = 0.6, 0.68$, $(\beta, \lambda) = (-5, 4)$. Hence, we expect such squirmer system to exhibit active turbulence. A characteristic length scale can also exist for lower densities, e.g., for $\phi = 0.4$, $(\beta, \lambda) = (-5, 0), (-5, 4)$, where only small clusters are present. We do not denote the dynamics of such systems as turbulent according to the criteria provided in the Discussion and Conclusions section.

Energy spectrum. Insight into the turbulent behavior is gained by the energy spectrum

$$E(k) = \frac{k}{2\pi} \int d^2 R \, e^{-i\mathbf{k}\cdot\mathbf{R}} C_v(\mathbf{R}), \tag{7}$$

which is obtained as Fourier transform of the spatial velocity correlation function (5)[47], and manifests the distribution of kinetic energy over different length scales. In the calculation of $E(k)$, we apply a left-shift of the correlation function $C_v(R)$ (Fig. 9) such that the decay starts at $R = 0$ in order to avoid artifacts in
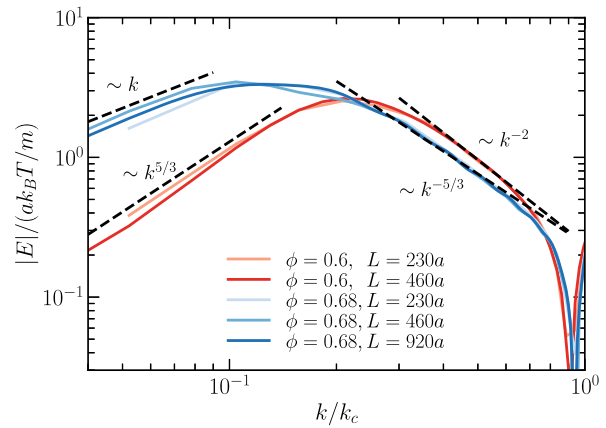
Fig. 10 Energy spectrum. Energy spectra of systems with the active stress $\beta = -5$ and rotlet-dipole strength $\lambda = 4$ for the packing fractions $\phi = 0.6$ (red) and 0.68 (blue) as a function fo the wave vector k, with $k_c = \pi/b_z$ and b_z the semi-major axis of the spheroidal colloid. Various system sizes, L, (see legend) have been explored in order to verify absence of finite-size effects. The dashed lines indicate power-laws in the respective regimes.

the Fourier transformation by a truncated correlation function. As for bacterial suspensions, the energy injection scale is the length scale of a microswimmer ($2b_z$), which yields the characteristic (maximum) wavenumber $k_c = \pi/b_z$ for our squirmers.

Figure 10 displays the energy spectrum for $(\beta, \lambda) = (-5, 4)$ and the two packing fractions $\phi = 0.6, 0.68$, and various system sizes. The simulations show two power-law regimes for a given density, namely $E(k) \sim k^{\hat{\kappa}}$ for $k < k_m$ and $E(k) \sim k^{-\kappa}$ for $k_m < k < k_c$, with k_m corresponding to the position of the maximum of $E(k)$. Such a maximum in $E(k)$ is a feature of microswimmer active turbulence, and reflects a characteristic vortex size[13,35,36]. Our simulations yield approximate vortex sizes of 5 ($10b_z$) and 10 squirmer lengths ($20b_z$) for $\phi = 0.6$ and 0.68, respectively. They are roughly consistent with the patterns of Fig. 8, the crossover from ballistic to diffusive motion in the mean-square displacement of Fig. 6, and the minimum of the correlation function of Fig. 9(b). Vortex sizes on the order of 5–10 microswimmer lengths are also found in experiments[13,35,38].

For $k_m < k < k_c$, corresponding to $R > 2b_x$, our simulations yield turbulent flow patterns (Fig. 8). The exponent of the scaling regime depends on the squirmer density, with the values $\kappa = -2$ for $\phi = 0.6$ and $\kappa = -5/3$ for $\phi = 0.68$. The latter is consistent with the Kolmogorov-Kraichnan prediction for classical 2D turbulence[45]. This is in contrast to the wide range of exponents found in simulations and experiments (cf. Table 1). Density seems to play an important role for the observed turbulent behavior. The squirmers of both densities exhibit swarming motility, namely, collective motion with large-scale swirling and streaming patterns. However, only the dynamics in the higher density system exhibits the exponent $\kappa = 5/3$.

In the small k-value regime, we obtain the exponents $\hat{\kappa} = 1$ for $\phi = 0.68$ and $\hat{\kappa} = 5/3$ for $\phi = 0.6$, which reflect an increase of the energy with increasing k. The dependence $k^{5/3}$ is consistent with that observed theoretically and experimentally in Ref. [13], as well as in simulations[49]. However, other studies yield rather different dependencies (Table 1). Theoretical models suggest that the small-k slope is governed by finite-system-size effects, i.e., depends in the boundary condition and physical parameters[43]. The curves in Fig. 10 reflect a weak dependence on the system size.

The presences of a small-distance cut-off, where energy input by the squirmers occurs, and the peak in $E(k)$, corresponding to a characteristic vortex size, limits the k-range over which the energy

spectrum decays in a power-law manner. This is in stark contrast to classical high-Reynolds-number turbulence, where the energy cascade extents over many orders of magnitude.

Discussion

We have performed large-scale mesoscale hydrodynamics simulations of spheroidal squirmers in a narrow slit in order to analyze the emerging structures, motility patterns, and turbulent behavior for various packing fractions, active stresses, and rotlet-dipole strengths.

Our studies reveal a strong dependence of the motility pattern on the microswimmer concentration and their propulsion-induced flow field. The classification of the distinct motion pattern into the various categories — swimming and collective motion of very small clusters (cluster gas), phase separation by activity and anisotropic swimmer shape (A-MIPS), and swarming — is accomplished by visual inspection of snapshots (Fig. 2) and the characteristic features of the cluster-size distribution function (Fig. 4). A-MIPS appears for small active stresses, $|\beta| \lesssim 3$, and all packing fractions $\phi > 0.2$. Here, we expect enhanced cluster formation for larger system sizes rather than active turbulence. Squirmers with stronger forces dipoles, $|\beta| \gtrsim 3$, at concentrations $\phi < 0.4$ exhibit small clusters and strong cooperative effects for $\lambda = 4$. At higher packing fractions, $\phi > 0.6$, swarming motility appears for the rotlet-dipole strength $\lambda = 4$, where clusters of squirmers move collectively, and even exhibit active turbulence for $\phi = 0.68$ and $\beta = -5$ (Fig. 2). Importantly, the rotlet dipole suppresses A-MIPS. As shown in Fig. 10, this behavior is independent of system size.

Our simulations clearly reveal the difficulty to characterize turbulence in active systems. Even more fundamental is the question, which criteria should be applied to classify a mesoscale system as turbulent. Considering microswimmer systems, visually chaotic flow patterns are evidently not sufficient. Inspired by experimental systems displaying bacterial turbulence, our simulation results for squirmer, and systems exhibiting classical hydrodynamic turbulence, we propose the following "minimal" criteria for bacterial turbulence:

- Reynolds numbers $Re \ll 1$[10,13]
- high microswimmer density: closely packed swimmers with average distances smaller than their size[16]
- presence of visually chaotic flow patterns[18,43,52] with large-scale collective behavior
- characteristic vortex size[35,36] and a velocity correlation function which becomes negative on intermediate distances
- Gaussian velocity-distribution function of the microswimmer's Cartesian velocity components[13,36]
- energy spectrum with power-law decay $E(k) \sim k^{-\kappa}$, $\kappa > 0$, on length scales below the characteristic vortex size.

The presence of small and large length-scale cut-offs by the microswimmer and vortex size implies a universal, scale-free behavior only over a limited range of length scales.

Analyzing the swarming motion of the squirmers, we find non-Gaussian distribution functions for the velocities parallel to the confining walls for $\phi \leq 0.6$. According to our criteria, we classify such systems as non-turbulent. However, we obtain a Gaussian velocity distribution for $\phi = 0.68$ and $(\beta, \lambda) = (-5, 4)$ (Fig. 7). The energy spectrum of that system exhibits a power-law decay with the exponent $\kappa = 5/3$, characteristic for Kolmogorov-Kraichnan-type turbulence in the inertial range. Hence, this systems fulfills all the above criteria, and we consider it as fully turbulent.

The slope of the power-law regime depends on the squirmer density. At the smaller packing fraction $\phi = 0.6$ and $(\beta, \lambda) = (-5, 4)$, the energy spectrum decreases faster, with the exponent

$\kappa = 2$. At the same time, the velocity distribution function is non-Gaussian. Thus, the system is not showing active turbulence in the above sense, yet, is exhibiting swarming behavior. This suggests a tight link between the energy spectrum and the velocity distribution function, a relation which needs further considerations.

As typically observed in turbulent bacterial suspensions[13,35,36], we also obtain a maximum in the energy spectrum at 5–10 squirmer lengths, as well as a negative spatial velocity correlation function, in agreement with the presence of a characteristic vortex size.

The effective inertia due to the collective active motion could play an important role, since the crossover from the active ballistic motion — equivalent to inertia of a passive system — to active diffusion appears on the length scale of approximately 6 squirmers lengths, which is comparable to the characteristic vortex size. Yet, the Reynolds number on the scale of a vortex (approximately 10 microswimmer lengths) is still smaller than unity. Here, more detailed theoretical studies of a suitable model are required to assess the relevance of the various interactions on active turbulence.

Despite the similarities of our squirmer systems with bacterial suspensions, there is one major difference, namely, the swimming speed of bacteria increasing in the swarming phase, whereas it decreases in our case[88]. This may point toward a particular role of bacterial flagella in the propulsion of the dense bacterial system.

We like to emphasize that hydrodynamic interactions are paramount for microswimmer swarming and active turbulence, specifically the active stress and the rotlet dipole determine their swarming motility. However, for Kolmogorov-Kraichnan-type characteristics to emerge, in addition, density plays a major role, and ensures an isotropic and homogeneous dynamics on lengths scales larger than approximately a squirmer length. Our simulations provide a benchmark for further theoretical and simulation studies on bacterial turbulence to elucidate the interplay between hydrodynamic stress — specifically a rotlet dipole —, alignment interactions by anisotropic swimmer shapes, and volume exclusion.

Methods

Microswimmer model: prolate squirmer. The prescribed surface velocity of the prolate spheroidal squirmer, a homogeneous colloidal particle of mass M, is given by[61–64]

$$\boldsymbol{u}_s = -B_1(1 + \beta\zeta)(\boldsymbol{e}_\zeta \cdot \boldsymbol{e})\boldsymbol{e}_\zeta + \frac{3\lambda z_s \bar{r}_s}{r_s^5}\boldsymbol{e}_\varphi \qquad (8)$$

in terms of spheroidal coordinates τ, ζ, φ ($1 \leq \tau < \infty$, $-1 \leq \zeta \leq 1$, $0 \leq \varphi < 2\pi$) (Fig. 1(a))[63,89]. For a squirmer with propulsion direction $\boldsymbol{e} = (0, 0, 1)$, the Cartesian coordinates of a point on the spheroid surface $\boldsymbol{r}_s = (x_s, y_s, z_s)^T$ are

$$x_s = b_x\sqrt{1 - \zeta^2}\cos\varphi, \ y_s = b_x\sqrt{1 - \zeta^2}\sin\varphi, \ z_s = b_z\zeta,$$

with $\bar{r}_s = \sqrt{x_s^2 + y_s^2}$, $r_s = |\boldsymbol{r}_s|$, $\tau = \tau_0 = b_z/\sqrt{b_z^2 - b_x^2}$, and the lengths b_z and b_x along the semi-major and -minor axis (Fig. 1(a)). The terms with the coefficients B_1 and β ($\beta < 0$, pusher) account for swimming in the direction $\boldsymbol{e}$ and an active stress, respectively[63,77,89]. The rotlet-dipole term (second term on the right-hand side of Eq. (8)) accounts for the torque-free nature of swimming bacteria with a cell body counterrotating with respect to the flagellar bundle[66]. Equation (8) is a straightforward generalization of the expression derived for spheres with the independent parameter λ[90]. It is a solution of Stokes' equations and, with the boundary condition on the spheroid's surface (8), the velocity field of such a squirmer in an infinite fluid is given by $\boldsymbol{v}_R(\boldsymbol{r}) = 3\lambda z \bar{r} \boldsymbol{e}_\varphi / r^5$ in a reference frame, where $\boldsymbol{e}$ is aligned with the z axis of the body-fixed reference frame (see Fig. 1), $\bar{r} = \sqrt{x^2 + y^2}$, and $r = |\boldsymbol{r}|$. The swimming velocity of a squirmer is related to B_1 as

$$v_0 = B_1\tau_0[\tau_0 - (\tau_0^2 - 1)\coth^{-1}\tau_0]. \qquad (9)$$

To insure quasi-two-dimensional motion between the walls (Fig. 1(b)), a strong repulsive interaction between squirmers and walls is implemented by the truncated

and shifted Lennard-Jones potential

$$U_w = 4\epsilon_w \left[\left(\frac{\sigma_w}{y}\right)^{12} - \left(\frac{\sigma_w}{y}\right)^6 + \frac{1}{4} \right] \qquad (10)$$

for $y < 2^{1/6}\sigma_w$ and zero else, where y is the closest distance between a wall and the surface of a squirmer. Here, σ_w and ϵ_w determine to the length and energy scale, respectively. Hence, squirmers never touch a wall.

Squirmer volume-exclusion interactions are described by a separation-shifted Lennard-Jones potential with parameters σ_s and ϵ_s, where $y \rightarrow d_s + \sigma_s$ in Eq. (10), and d_s is the distance between the two closest points on the surfaces of two interacting spheroids[63,89].

The solid-body equations of motion of the squirmers — the center-of-mass translational motion and the rotational motion described by quaternions — are solved by the velocity-Verlet algorithm[63,89].

Fluid model: multiparticle collision dynamics. The fluid is modeled via the multiparticle collision dynamics (MPC) method, a particle-based mesoscale simulation approach accounting for thermal fluctuations[58,59], which has been shown to correctly capture hydrodynamic interactions[91], specifically for active agents and systems[66,90,92-101].

We apply the MPC approach with angular momentum conservation (MPC-SRD+a)[77,78]. The algorithm proceeds in two steps — streaming and collision. In the streaming step, the MPC point particles of mass m propagate ballistically over a time interval h, denoted as collision time. In the collision step, fluid particles are sorted into the cells of a cubic lattice of lattice constant a defining the collision environment, and their relative velocities, with respect to the center-of-mass velocity of the collision cell, are rotated around a randomly oriented axes by a fixed angle α. The algorithm conserves mass, linear, and angular momentum on the collision-cell level, which implies hydrodynamics on large length and long time scales[58,91]. A random shift of the collision cell lattice is applied at every collision step to ensure Galilean invariance[102]. Thermal fluctuations are intrinsic to the MPC method. A cell-level canonical thermostat (Maxwell-Boltzmann scaling (MBS) thermostat) is applied after every collision step, which maintains the temperature at the desired value[103]. The MPC method is highly parallel and is efficiently implemented on a graphics processing unit (GPU) for a high-performance gain[104].

The fluid and the squirmers are confined in a narrow slit with no-slip boundary conditions of the fluid at the walls. Squirmer-fluid interactions appear during streaming and collision. While streaming squirmers and fluid particles, fluid particles are reflected at a squirmer's surface by application of the bounce-back rule and addition of the surface velocity $\boldsymbol{u}_s$(8). To minimize slip, phantom particles are added inside of the squirmers, which contribute when collision cells penetrate squirmers. In all cases, the total linear and angular momenta are included in the squirmer dynamics. More details are described in Ref. [63] and the supplementary material of Ref. [89].

Parameters. Multiple squirmers with the semi-major axis $b_z = 6a$ and semi-minor axis $b_x = 2a$ are distributed in a narrow slit of width $L_y = 8a$, where a is the length of the MPC fluid collision cell. Parallel to the walls, periodic boundary conditions are applied. We set $\sigma_w = 1.8a$ and $\epsilon_w = 18k_BT$. Squirmer propulsion requires fluid particles adjacent to its surface. To avoid MPC particle depletion when two squirmers approach each other, we introduce a safety layer of thickness $d_v = 0.25a$ around every squirmer, corresponding to the effective squirmer semi-axes $b_z + d_v$ and $b_x + d_v$, respectively. The squirmer-squirmer Lennard-Jones parameters are set to $\sigma_s = 0.5a$, $\epsilon_s = 5k_BT$. d_s (see microswimmer model) is now the distance between two closest points on the surfaces of the two interacting squirmers with effective (larger) semi-axes[60,63,89].

We employ a high average particle number $\langle N_c \rangle = 60$ in a collision cell[60]. Furthermore, we choose a small collision-time step $h = 0.02\sqrt{ma^2/(k_BT)}$ and the large rotation angle $\alpha = 130°$. This results in the fluid viscosity $\eta = 127.8\sqrt{mk_BT/a^4}$ and the 2D rotational diffusion coefficient around a minor axis $D_R^0 = 5.2 \times 10^{-6}\sqrt{k_BT/(ma^2)}$. This is in close agreement with the theoretical value of a spheroid $D_R^0 = 5.5 \times 10^{-6}\sqrt{k_BT/(ma^2)}$.

For a squirmer, we choose $B_1 = 4.5 \times 10^{-3}\sqrt{k_BT/m}$, corresponding to the swimming speed $v_0 = 4 \times 10^{-3}\sqrt{k_BT/m}$, which yields the Péclet number $Pe = v_0/(2b_zD_R^0) = 64$ and the Reynolds number $Re = 2b_zv_0 \langle N_c \rangle /(a^3\eta) = 0.023$. The active stress values $\beta = -1, -3, -5$, covering approximately the estimated values from experiments and simulations (see below), and the rotlet dipole strengths $\lambda = 0, 4$ are considered. Typically, simulations with the box size $L = 160a$ are performed for the 2D packing fractions $\phi = N_{sq}\pi b_xb_z/L^2 = 0.1, 0.2, 0.3, 0.4,$ and 0.5, corresponding to the squirmer numbers $N_{sq} = 66, 140, 200, 270,$ and 341. In order to reduce/avoid finite-size effects and to confirm our conclusions, we considered other system sizes, specifically, for higher densities significantly larger systems are simulated with $L = 230a$ for $N_{sq} = 833, 954$, $L = 460a$ and $N_{sq} = 3332, 3816$ (both $\phi = 0.6, 0.68$), as well as $L = 920a$ for $N_{sq} = 15264$ ($\phi = 0.68$). (Note that the largest system contains 4×10^8 MPC fluid particles.) A passive spheroid is neutrally bouyant with $M = 6031m$, and the MPC time step h is used in the integration of the squirmers' equations of motion. Presented data are collected over the total time interval $10^6\sqrt{ma^2/(k_BT)}$, after an extended equilibration period where the systems reached a stationary state. During this time, in dilute solution a squirmer actively diffuses about 150 body lengths, which corresponds to twice the size of the largest system, while for the largest packing fraction a squirmer travels about 1/3 of the system size.

Estimation of squirmer parameters for E. coli from simulations and experiments. In the far-field, the microswimmer flow field is dominated by the force-dipole term of strength[6,15,65,105]

$$\chi = \frac{P}{8\pi\eta}, \qquad (11)$$

where $P = f_Dl_D$ is the magnitude of the force dipole of force f_D and length l_D. The latter parameters can be determined from experiments[65] and simulations[66]. The far-field expansion of the flow field of a spheroidal squirmer provides the relation between χ and the active stress parameter β[63]:

$$\beta = -\frac{\chi}{v_0(b_z^2 - b_x^2)} \frac{[3\tau_0 + (1 - 3\tau_0^2)\coth^{-1}\tau_0][\tau_0 - (\tau_0^2 - 1)\coth^{-1}\tau_0]}{2/3 - \tau_0^2 + \tau_0(\tau_0^2 - 1)\coth^{-1}\tau_0}. \qquad (12)$$

With the approximation of the bacteria cell body by a spheroid, Eq. (12) provides an estimation of β for a given χ.

- *From simulations* — An E. coli-type cell model with the body length $l_b = 2.4\mu m$, cell body diameter $d_b = 0.9\mu m$, the swimming speed $v_0 = 40\mu m/s$, force-dipole strength $f_D = 0.57pN$, and force-dipole length $l_D = 3.84\mu m$[66], yields $\beta \approx -6$. We use the cell body length rather the length of body plus flagellar bundle, guided by the discussion of E. coli rotation in Ref. [65].

- *From experiments* — E. coli bacteria are characterized by $l_b = 3\,\mu m$, $d_b = 1\,\mu m$, $v_0 = 22\,\mu m/s$, $f_D = 0.42\,pN$, and $l_D = 1.9\,\mu m$[65], which gives $\beta \approx -3$.

In both cases, the viscosity of water is used. These β values approximately fall into the range of active stresses considered in our simulations.

Data availability

The data that support the findings of this study are available from the corresponding author upon reasonable request.

Code availability

The custom code for the simulations on GPUs is available from the corresponding author upon reasonable request.

References

1. Vicsek, T. & Zafeiris, A. Collective motion. *Phys. Rep.* **517**, 71 (2012).
2. Toner, J. & Tu, Y. Long-range order in a two-dimensional dynamical xy model: How birds fly together. *Phys. Rev. Lett.* **75**, 4326 (1995).
3. Cavagna, A. & Giardina, I. Bird flocks as condensed matter. *Annu. Rev. Condens. Matter Phys.* **5**, 183 (2014).
4. Chaté, H. Dry aligning dilute active matter. *Annu. Rev. Condens. Matter Phys.* **11**, 189 (2020).
5. Ward, A. J. W., Sumpter, D. J. T., Couzin, I. D., Hart, P. J. B. & Krause, J. Quorum decision-making facilitates information transfer in fish shoals. *Proc. Natl Acad. Sci. USA* **105**, 6948 (2008).
6. Shaebani, M. R., Wysocki, A., Winkler, R. G., Gompper, G. & Rieger, H. Computational models for active matter. *Nat. Rev. Phys.* **2**, 181 (2020).
7. Henrichsen, J. Bacterial surface translocation: a survey and a classification. *Bacteriol. Rev.* **36**, 478 (1972).
8. Sokolov, A., Aranson, I. S., Kessler, J. O. & Goldstein, R. E. Concentration dependence of the collective dynamics of swimming bacteria. *Phys. Rev. Lett.* **98**, 158102 (2007).
9. Berg, H. C., *E. coli in motion, biological and medical physics series* (Springer, New York, 2004).
10. Copeland, M. F. & Weibel, D. B. Bacterial swarming: a model system for studying dynamic self-assembly. *Soft Matter* **5**, 1174 (2009).
11. Darnton, N. C., Turner, L., Rojevsky, S. & Berg, H. C. Dynamics of bacterial swarming. *Biophys. J.* **98**, 2082 (2010).
12. Kearns, D. B. A field guide to bacterial swarming motility. *Nat. Rev. Microbiol.* **8**, 634 (2010).
13. Wensink, H. H. et al. Meso-scale turbulence in living fluids. *Proc. Natl Acad. Sci. USA* **109**, 14308 (2012).
14. Marchetti, M. C. et al. Hydrodynamics of soft active matter. *Rev. Mod. Phys.* **85**, 1143 (2013).

15. Elgeti, J., Winkler, R. G. & Gompper, G. Physics of microswimmers—single particle motion and collective behavior: a review. *Rep. Prog. Phys.* **78**, 056601 (2015).

16. Be'er, A. et al. A phase diagram for bacterial swarming. *Commun. Phys.* **3**, 66 (2020).

17. Hakim, V. & Silberzan, P. Collective cell migration: a physics perspective. *Rep. Prog. Phys.* **80**, 076601 (2017).

18. Alert, R., Joanny, J.-F. & Casademunt, J. Universal scaling of active nematic turbulence. *Nat. Phys.* **16**, 682 (2020).

19. Tan, T. H. et al. Topological turbulence in the membrane of a living cell. *Nat. Phys.* **16**, 657 (2020).

20. Jülicher, F., Kruse, K., Prost, J. & Joanny, J.-F. Active behavior of the cytoskeleton. *Phys. Rep.* **449**, 3 (2007).

21. Needleman, D. & Dogic, Z. Active matter at the interface between materials science and cell biology. *Nat. Rev. Mater.* **2**, 17048 (2017).

22. Doostmohammadi, A., Ignés-Mullol, J., Yeomans, J. M. & Sagués, F. Active nematics. *Nat. Commun.* **9**, 3246 (2018).

23. Opathalage, A. et al. Self-organized dynamics and the transition to turbulence of confined active nematics. *Proc. Natl Acad. Sci. USA* **116**, 4788 (2019).

24. Chamanbaz, M. et al. Swarm-enabling technology for multi-robot systems. *Front. Robot. AI* **4**, 12 (2017).

25. Rubenstein, M., Cornejo, A. & Nagpal, R. Programmable self-assembly in a thousand-robot swarm. *Science* **345**, 795 (2014).

26. Kokot, G. et al. Active turbulence in a gas of self-assembled spinners. *Proc. Natl Acad. Sci. USA* **114**, 12870 (2017).

27. Cohen, J. A. & Golestanian, R. Emergent cometlike swarming of optically driven thermally active colloids. *Phys. Rev. Lett.* **112**, 068302 (2014).

28. Bourgoin, M. et al. Kolmogorovian active turbulence of a sparse assembly of interacting marangoni surfers. *Phy. Rev. X* **10**, 021065 (2020).

29. Gompper, G. et al. The 2020 motile active matter roadmap. *J. Phys: Condens. Matter* **32**, 193001 (2020).

30. Turner, L., Zhang, R., Darnton, N. C. & Berg, H. C. Visualization of flagella during bacterial swarming. *J. Bacteriol.* **192**, 3259 (2010).

31. Be'er, A. & Ariel, G. A statistical physics view of swarming bacteria. *Mov. Ecol.* **7**, 9 (2019).

32. Dombrowski, C., Cisneros, L., Chatkaew, S., Goldstein, R. E. & Kessler, J. O. Self-concentration and large-scale coherence in bacterial dynamics. *Phys. Rev. Lett.* **93**, 098103 (2004).

33. Wolgemuth, C. W. Collective swimming and the dynamics of bacterial turbulence. *Biophys. J.* **95**, 1564 (2008).

34. Zhang, H. P., Be'er, A., Smith, R. S., Florin, E. L., & Swinney, H. L. Swarming dynamics in bacterial colonies. *Europhys. Lett.* **87**, 48011 (2009).

35. Sokolov, A. & Aranson, I. S. Physical properties of collective motion in suspensions of bacteria. *Phys. Rev. Lett.* **109**, 248109 (2012).

36. Dunkel, J., Heidenreich, S., Drescher, K., Wensink, H. H., Bär, M. & Goldstein, R. E. Fluid dynamics of bacterial turbulence. *Phys. Rev. Lett.* **110**, 228102 (2013).

37. Ryan, S. D., Sokolov, A., Berlyand, L. & Aranson, I. S. Correlation properties of collective motion in bacterial suspensions. *N. J. Phys.* **15**, 105021 (2013).

38. Beppu, K. et al. Geometry-driven collective ordering of bacterial vortices. *Soft Matter* **13**, 5038 (2017).

39. Poujade, M. et al. Collective migration of an epithelial monolayer in response to a model wound. *Proc. Natl Acad. Sci. USA* **104**, 15988 (2007).

40. Doostmohammadi, A. et al. Celebrating soft matter's 10th anniversary: cell division: a source of active stress in cellular monolayers. *Soft Matter* **11**, 7328 (2015).

41. Lin, S.-Z., Zhang, W.-Y., Bi, D., Li, B. & Feng, X.-Q. Energetics of mesoscale cell turbulence in two-dimensional monolayers. *Commun. Phys.* **4**, 21 (2021).

42. Giomi, L. Geometry and topology of turbulence in active nematics. *Phy. Rev. X* **5**, 031003 (2015).

43. Bratanov, V., Jenko, F. & Frey, E. New class of turbulence in active fluids. *Proc. Natl Acad. Sci. USA* **112**, 15048 (2015).

44. Kolmogorov, A. N., Levin, V., Hunt, J. C. R., Phillips, O. M. & Williams, D. The local structure of turbulence in incompressible viscous fluid for very large Reynolds numbers. *Proc. R. Soc. A* **434**, 9 (1991).

45. Kraichnan, R. H. & Montgomery, D. Two-dimensional turbulence. *Rep. Prog. Phys.* **43**, 547 (1980).

46. Frisch, U. & Kolmogorov, A. N. *Turbulence: the legacy of A. N. Kolmogorov* (Cambridge University Press, 1995).

47. Batchelor, G. K. *The theory of homogeneous turbulence.* (University Press, Cambridge, 1959).

48. Vicsek, T., Czirók, A., Ben-Jacob, E., Cohen, I. & Shochet, O. Novel type of phase transition in a system of self-driven particles. *Phys. Rev. Lett.* **75**, 1226 (1995).

49. Großmann, R., Romanczuk, P., Bär, M. & Schimansky-Geier, L. Vortex arrays and mesoscale turbulence of self-propelled particles. *Phys. Rev. Lett.* **113**, 258104 (2014).

50. Wensink, H. H. & Löwen, H. Emergent states in dense systems of active rods: from swarming to turbulence. *J. Phys. Condens. Matter* **24**, 460130 (2012).

51. Bárdfalvy, D., Nordanger, H., Nardini, C., Morozov, A. & Stenhammar, J. Particle-resolved lattice Boltzmann simulations of 3-dimensional active turbulence. *Soft Matter* **15**, 7747 (2019).

52. Doostmohammadi, A., Shendruk, T. N., Thijssen, K. & Yeomans, J. M. Onset of meso-scale turbulence in active nematics. *Nat. Commun.* **8**, 15326 (2017).

53. Kokot, G., Piet, D., Whitesides, G. M., Aranson, I. S. & Snezhko, A. Emergence of reconfigurable wires and spinners via dynamic self-assembly. *Sci. Rep.* **5**, 9528 (2015).

54. Reinken, H., Klapp, S. H. L., Bär, M. & Heidenreich, S. Derivation of a hydrodynamic theory for mesoscale dynamics in microswimmer suspensions. *Phys. Rev. E* **97**, 022613 (2018).

55. Toner, J. & Tu, Y. Flocks, herds, and schools: A quantitative theory of flocking. *Phys. Rev. E* **58**, 4828 (1998).

56. Ramaswamy, S. The mechanics and statistics of active matter. *Annu. Rev. Cond. Mat. Phys.* **1**, 323 (2010).

57. Swift, J. & Hohenberg, P. C. Hydrodynamic fluctuations at the convective instability. *Phys. Rev. A* **15**, 319 (1977).

58. Kapral, R. Multiparticle collision dynamics: simulations of complex systems on mesoscale. *Adv. Chem. Phys.* **140**, 89 (2008).

59. Gompper, G., Ihle, T., Kroll, D. M. & Winkler, R. G. Multi-particle collision dynamics: a particle-based mesoscale simulation approach to the hydrodynamics of complex fluids. *Adv. Polym. Sci.* **221**, 1 (2009).

60. Theers, M., Westphal, E., Qi, K., Winkler, R. G. & Gompper, G. Clustering of microswimmers: interplay of shape and hydrodynamics. *Soft Matter* **14**, 8590 (2018).

61. Ishikawa, T., Simmonds, M. P. & Pedley, T. J. Hydrodynamic interaction of two swimming model micro-organisms. *J. Fluid Mech.* **568**, 119 (2006).

62. Pagonabarraga, I. & Llopis, I. The structure and rheology of sheared model swimmer suspensions. *Soft Matter* **9**, 7174 (2013).

63. Theers, M., Westphal, E., Gompper, G. & Winkler, R. G. Modeling a spheroidal microswimmer and cooperative swimming in a narrow slit. *Soft Matter* **12**, 7372 (2016).

64. Zöttl, A. & Stark, H. Simulating squirmers with multiparticle collision dynamics. *Eur. Phys. J. E* **41**, 61 (2018).

65. Drescher, K., Dunkel, J., Cisneros, L. H., Ganguly, S. & Goldstein, R. E. Fluid dynamics and noise in bacterial cell-cell and cell-surface scattering. *Proc. Natl Acad. Sci. USA* **108**, 10940 (2011).

66. Hu, J., Yang, M., Gompper, G. & Winkler, R. G. Modelling the mechanics and hydrodynamics of swimming E. coli. *Soft Matter* **11**, 7867 (2015a).

67. Lopez, D. & Lauga, E. Dynamics of swimming bacteria at complex interfaces. *Phys. Fluids* **26**, 071902 (2014).

68. Ishimoto, K., Gaffney, E. A. & Walker, B. J. Regularized representation of bacterial hydrodynamics. *Phys. Rev. Fluids* **5**, 093101 (2020).

69. Kyoya, K., Matsunaga, D., Imai, Y., Omori, T. & Ishikawa, T. Shape matters: Near-field fluid mechanics dominate the collective motions of ellipsoidal squirmers. *Phys. Rev. E* **92**, 063027 (2015).

70. Cates, M. E. & Tailleur, J. Motility-induced phase separation. *Annu. Rev. Condens. Matter Phys.* **6**, 219 (2015).

71. Bechinger, C. et al. Active particles in complex and crowded environments. *Rev. Mod. Phys.* **88**, 045006 (2016).

72. Bialké, J., Speck, T. & Löwen, H. Crystallization in a dense suspension of self-propelled particles. *Phys. Rev. Lett.* **108**, 168301 (2012).

73. Redner, G. S., Hagan, M. F. & Baskaran, A. Structure and dynamics of a phase-separating active colloidal fluid. *Phys. Rev. Lett.* **110**, 055701 (2013).

74. Wysocki, A., Winkler, R. G. & Gompper, G. Cooperative motion of active Brownian spheres in three-dimensional dense suspensions. *EPL* **105**, 48004 (2014).

75. Digregorio, P. et al. Full phase diagram of active Brownian disks: from melting to motility-induced phase separation. *Phys. Rev. Lett.* **121**, 098003 (2018).

76. Matas-Navarro, R., Golestanian, R., Liverpool, T. B. & Fielding, S. M. Hydrodynamic suppression of phase separation in active suspensions. *Phys. Rev. E* **90**, 032304 (2014).

77. Theers, M., Westphal, E., Gompper, G. & Winkler, R. G. From local to hydrodynamic friction in Brownian motion: A multiparticle collision dynamics simulation study. *Phys. Rev. E* **93**, 032604 (2016).

78. Noguchi, H. & Gompper, G. Transport coefficients of off-lattice mesoscale-hydrodynamics simulation techniques. *Phys. Rev. E* **78**, 016706 (2008).

79. Rycroft, C. H. VORO++: A three-dimensional Voronoi cell library in C++. *Chaos* **19**, 041111 (2009).

80. Persson, P. & Strang, G. A simple mesh generator in matlab. *SIAM Rev.* **46**, 329 (2004).

81. Levis, D. & Berthier, L. Clustering and heterogeneous dynamics in a kinetic monte carlo model of self-propelled hard disks. *Phys. Rev. E* **89**, 062301 (2014).

82. Alarcón, F., Valeriani, C. & Pagonabarraga, I. Morphology of clusters of attractive dry and wet self-propelled spherical particle suspensions. *Soft Matter* **13**, 814 (2017).

83. Ginot, F., Theurkauff, I., Detcheverry, F., Ybert, C. & Cottin-Bizonne, C. Aggregation-fragmentation and individual dynamics of active clusters. *Nat. Commun.* **9**, 696 (2018).

84. Caprini, L. & Marini Bettolo Marconi, U. Active matter at high density: Velocity distribution and kinetic temperature. *J. Chem. Phys.* **153**, 184901 (2020).

85. Wu, P.-H., Giri, A., Sun, S. X. & Wirtz, D. Three-dimensional cell migration does not follow a random walk. *Proc. Natl Acad. Sci. USA* **111**, 3949 (2014).

86. Souza Vilela Podestá, T., Venzel Rosembach, T., Aparecida dos Santos, A. & Lobato Martins, M. Anomalous diffusion and q-weibull velocity distributions in epithelial cell migration. *PLOS One* **12**, e0180777 (2017).

87. Chen, X., Dong, X., Be'er, A., Swinney, H. L. & Zhang, H. P. Scale-invariant correlations in dynamic bacterial clusters. *Phys. Rev. Lett.* **108**, 148101 (2012).

88. Swiecicki, J.-M., Sliusarenko, O. & Weibel, D. B. From swimming to swarming: Escherichia coli cell motility in two-dimensions. *Integr. Biol.* **5**, 1490 (2013).

89. Qi, K., Westphal, E., Gompper, G. & Winkler, R. G. Enhanced rotational motion of spherical squirmer in polymer solutions. *Phys. Rev. Lett.* **124**, 068001 (2020).

90. Pak, O. S. & Lauga, E. Generalized squirming motion of a sphere. *J. Eng. Math.* **88**, 1 (2014).

91. Huang, C.-C., Gompper, G. & Winkler, R. G. Hydrodynamic correlations in multiparticle collision dynamics fluids. *Phys. Rev. E* **86**, 056711 (2012).

92. Goldstein, R. E., Polin, M. & Tuval, I. Noise and Synchronization in Pairs of Beating Eukaryotic Flagella. *Phys. Rev. Lett.* **103**, 168103 (2009).

93. Reigh, S. Y., Winkler, R. G. & Gompper, G. Synchronization and bundling of anchored bacterial flagella. *Soft Matter* **8**, 4363 (2012).

94. Geyer, V. F., Jülicher, F., Howard, J. & Friedrich, B. M. Cell-body rocking is a dominant mechanism for flagellar synchronization in a swimming alga. *Proc. Natl Acad. Sci. USA* **110**, 18058 (2013).

95. Brumley, D. R., Wan, K. Y., Polin, M. & Goldstein, R. E. Flagellar synchronization through direct hydrodynamic interactions. *eLife* **3**, e02750 (2014).

96. Theers, M. & Winkler, R. G. Effects of thermal fluctuations and fluid compressibility on hydrodynamic synchronization of microrotors at finite oscillatory Reynolds number: A multiparticle collision dynamics simulation study. *Soft Matter* **10**, 5894 (2014).

97. Eisenstecken, T., Gompper, G. & Winkler, R. G. Conformational properties of active semiflexible polymers. *Polymers* **8**, 304 (2016).

98. Hu, J., Wysocki, A., Winkler, R. G. & Gompper, G. Physical sensing of surface properties by microswimmers – directing bacterial motion via wall slip. *Sci. Rep.* **5**, 9586 (2015b).

99. Mousavi, S. M., Gompper, G. & Winkler, R. G. Wall entrapment of peritrichous bacteria: a mesoscale hydrodynamics simulation study. *Soft Matter* **16**, 4866 (2020).

100. Babu, S. B. & Stark, H. Modeling the locomotion of the african trypanosome using multi-particle collision dynamics. *N. J. Phys.* **14**, 085012 (2012).

101. Rode, S., Elgeti, J. & Gompper, G. Sperm motility in modulated microchannels. *N. J. Phys.* **21**, 013016 (2019).

102. Ihle, T. & Kroll, D. M. Stochastic rotation dynamics I: Formalism, Galilean invariance, Green-Kubo relations. *Phys. Rev. E* **67**, 066705 (2003).

103. Huang, C.-C., Chatterji, A., Sutmann, G., Gompper, G. & Winkler, R. G. Cell-level canonical sampling by velocity scaling for multiparticle collision dynamics simulations. *J. Comput. Phys.* **229**, 168 (2010).

104. Westphal, E., Singh, S. P., Huang, C.-C., Gompper, G. & Winkler, R. G. Multiparticle collision dynamics: GPU accelerated particle-based mesoscale hydrodynamic simulations. *Comput. Phys. Comm.* **185**, 495 (2014).

105. Lauga, E. & Powers, T. R. The hydrodynamics of swimming microorganisms. *Rep. Prog. Phys.* **72**, 096601 (2009).

Author contributions

R.G.W. and G.G. designed the study. K.Q. and E.W. wrote the simulation code and K.Q. performed the simulations. K.Q., R.G.W, and G.G. analyzed and discussed the results. R.G.W., G.G., and K.Q. wrote the paper.

Competing interests

The authors declare no competing interests.

Additional information

Supplementary information The online version contains supplementary material available at https://doi.org/10.1038/s42005-022-00820-7.

Correspondence and requests for materials should be addressed to Gerhard Gompper or Roland G. Winkler.

Reprints and permission information is available at http://www.nature.com/reprints

Publisher's note Springer Nature remains neutral with regard to jurisdictional claims in published maps and institutional affiliations.